

of Pacific trade wind slackening predicted under future climate warming should extend the 20th-century contraction of the OMZ into this century. This wind-driven forcing may eventually be overwhelmed by the stratification-driven deoxygenation of the ocean as a whole, as proxies of anoxia from Pleistocene sediments point to a larger tropical OMZ and greater N loss during warm climates (19, 34, 35). The relative influence of these effects and the time scales over which they operate on the tropical OMZ remain unknown.

The predominant 20th-century contraction of the North Pacific OMZ has important implications for the basin's N cycle. Over centennial time scales, the slowing pace of N loss would have reduced the NO_3^- deficit relative to plankton PO_4^{3-} requirements throughout surface waters of the N-limited North Pacific. Recent isotopic analysis of skeleton material from deep-sea corals near Hawaii also exhibit a decreasing trend over this time period, which has been interpreted as a signal of increasing N inputs from N_2 fixation (36). However, because isotopic and stoichiometric signals of denitrification are transported from the anoxic zone into the subtropical gyre (37), the reported coral trends may originate partly from the OMZ. Any remaining signal attributable to N_2 fixation would imply that the ecological niche of diazotrophs in the central gyre is uncoupled from the major N loss in the OMZ (38), and that a substantial imbalance of the Pacific N budget has persisted over the 20th century.

REFERENCES AND NOTES

1. R. Vaquer-Sunyer, C. M. Duarte, *Proc. Natl. Acad. Sci. U.S.A.* **105**, 15452–15457 (2008).
2. L. Bopp, C. Le Quere, M. Heimann, A. C. Manning, P. Monfray, *Global Biogeochem. Cycles* **16**, 6–1–6–13 (2002).
3. R. J. Matear, A. C. Hirst, *Global Biogeochem. Cycles* **17**, 1125 (2003).
4. F. Chan et al., *Science* **319**, 920 (2008).
5. R. J. Diaz, *J. Environ. Qual.* **30**, 275–281 (2001).
6. J. A. Koslow, J. Couture, *Nature* **502**, 163–164 (2013).
7. R. E. Keeling, A. Körtzinger, N. Gruber, *Annu. Rev. Mar. Sci.* **2**, 199–229 (2010).
8. L. Stramma, G. C. Johnson, J. Sprintall, V. Mohrholz, *Science* **320**, 655–658 (2008).
9. L. Bopp et al., *Biogeosciences* **10**, 6225–6245 (2013).
10. C. Deutsch, H. Brix, T. Ito, H. Frenzel, L. Thompson, *Science* **333**, 336–339 (2011).
11. T. Ito, C. Deutsch, *Global Biogeochem. Cycles* **27**, 1119–1128 (2013).
12. S. McClatchie, R. Goericke, R. Cosgrove, G. Auer, R. Vetter, *Geophys. Res. Lett.* **37**, L19602 (2010).
13. L. A. Codispoti, J. P. Christensen, *Mar. Chem.* **16**, 277–300 (1985).
14. J. A. Brandes, A. H. Devol, T. Yoshinari, D. A. Jayakumar, S. W. A. Naqvi, *Limnol. Oceanogr.* **43**, 1680–1689 (1998).
15. K. Kritee et al., *Geochim. Cosmochim. Acta* **92**, 243–259 (2012).
16. M. A. Altabet, *J. Geophys. Res.* **94**, 12771 (1989).
17. D. M. Sigman, K. L. Casciotti, in *Encyclopedia of Ocean Sciences*, J. H. Steele, K. H. Turekian, S. A. Thorpe, Eds. (Academic Press, London, 2001), vol. 4, pp. 1884–1894.
18. R. C. Thunell, D. M. Sigman, F. Muller-Karger, Y. Astor, R. Varela, *Global Biogeochem. Cycles* **18**, GB3001 (2004).
19. R. S. Ganeshram, T. F. Pedersen, S. E. Calvert, G. W. McNeill, M. R. Fontugne, *Paleoceanography* **15**, 361–376 (2000).
20. M. A. Altabet, M. J. Higginson, D. W. Murray, *Nature* **415**, 159–162 (2002).
21. See supplementary materials on Science Online.
22. C. G. Castro, F. P. Chavez, C. A. Collins, *Global Biogeochem. Cycles* **15**, 819–830 (2001).
23. S. S. Kienast, S. E. Calvert, T. F. Pedersen, *Paleoceanography* **17**, 7–17 (2002).
24. M. F. Lehmann, S. M. Bernasconi, A. Barbieri, J. A. McKenzie, *Geochim. Cosmochim. Acta* **66**, 3573–3584 (2002).
25. M. G. Prokopenko et al., *Earth Planet. Sci. Lett.* **242**, 186–204 (2006).
26. T. DeVries, C. Deutsch, F. Primeau, B. X. Chang, A. H. Devol, *Nat. Geosci.* **5**, 547–550 (2012).
27. J. I. Antonov, et al., in *NOAA Atlas NESDros. Inf. Serv.* 66 (U.S. Government Printing Office, Washington, DC, 2010).
28. G. A. Vecchi et al., *Nature* **441**, 73–76 (2006).
29. H. Tokinaga, S.-P. Xie, C. Deser, Y. Kosaka, Y. M. Okumura, *Nature* **491**, 439–443 (2012).
30. M. A. Merrifield, *J. Clim.* **24**, 4126–4138 (2011).
31. T. Ito, C. Deutsch, *Geophys. Res. Lett.* **37**, L03601 (2010).
32. T. M. Smith, R. W. Reynolds, T. C. Peterson, J. Lawrimore, *J. Clim.* **21**, 2283–2296 (2008).
33. M. H. England et al., *Nature Clim. Change* **4**, 222–227 (2014).
34. A. van Geen et al., *Paleoceanography* **18**, 1098 (2003).
35. S. L. Jaccard, E. D. Galbraith, *Nat. Geosci.* **5**, 151–156 (2012).
36. O. A. Sherwood, T. P. Guilderson, F. C. Batista, J. T. Schiff, M. D. McCarthy, *Nature* **505**, 78–81 (2014).
37. D. M. Sigman, P. J. DiFiore, M. P. Hain, C. Deutsch, D. M. Karl, *Geophys. Res. Lett.* **36**, L08605 (2009).
38. T. Weber, C. Deutsch, *Proc. Natl. Acad. Sci. U.S.A.* **111**, 8741–8746 (2014).
39. R. Allan, T. Ansell, *J. Clim.* **19**, 5816–5842 (2006).
40. S. M. Uppala et al., *Q. J. R. Meteorol. Soc.* **131**, 2961 (2005).

ACKNOWLEDGMENTS

This work was supported by grants from the National Science Foundation (OCE-0851483 to C.D.; OCE-1242313 to T.I.; OCE-0727123 to W.B.; OCE-0624777 to J.M.), by the Gordon and Betty Moore Foundation through Grant GBMF3775 to C.D., and by the U.S. Geological Survey Coastal and Marine Geology Program (J.C.). A grant from the Climate Center of Lamont-Doherty Earth Observatory (LDEO) contributed to the collection and dating of the Soledad Basin core. This is LDEO contribution number 7812.

SUPPLEMENTARY MATERIALS

www.sciencemag.org/content/345/6197/665/suppl/DC1
Materials and Methods
Figs. S1 to S8
References

17 February 2014; accepted 1 July 2014
10.1126/science.1252332

ARTIFICIAL BRAINS

A million spiking-neuron integrated circuit with a scalable communication network and interface

Paul A. Merolla,^{1*} John V. Arthur,^{1*} Rodrigo Alvarez-Icaza,^{1*} Andrew S. Cassidy,^{1*} Jun Sawada,^{2*} Filipp Akopyan,^{1*} Bryan L. Jackson,^{1*} Nabil Imam,³ Chen Guo,⁴ Yutaka Nakamura,⁵ Bernard Brezzo,⁶ Ivan Vo,² Steven K. Esser,¹ Rathinakumar Appuswamy,¹ Brian Taba,¹ Arnon Amir,¹ Myron D. Flickner,¹ William P. Risk,¹ Rajit Manohar,⁷ Dharmendra S. Modha^{1†}

Inspired by the brain's structure, we have developed an efficient, scalable, and flexible non-von Neumann architecture that leverages contemporary silicon technology. To demonstrate, we built a 5.4-billion-transistor chip with 4096 neurosynaptic cores interconnected via an intrachip network that integrates 1 million programmable spiking neurons and 256 million configurable synapses. Chips can be tiled in two dimensions via an interchip communication interface, seamlessly scaling the architecture to a cortexlike sheet of arbitrary size. The architecture is well suited to many applications that use complex neural networks in real time, for example, multiobject detection and classification. With 400-pixel-by-240-pixel video input at 30 frames per second, the chip consumes 63 milliwatts.

A long-standing dream (1, 2) has been to harness neuroscientific insights to build a versatile computer that is efficient in terms of energy and space, homogeneously scalable to large networks of neurons and synapses, and flexible enough to run complex

behavioral models of the neocortex (3, 4) as well as networks inspired by neural architectures (5).

No such computer exists today. The von Neumann architecture is fundamentally inefficient and nonscalable for representing massively interconnected neural networks (Fig. 1) with respect to computation, memory, and communication (Fig. 1B). Mixed analog-digital neuromorphic approaches have built large-scale systems (6–8) to emulate neurobiology by using custom computational elements, for example, silicon neurons (9, 10), winner-take-all circuits (11), and sensory circuits (12). We have found that a multiplexed digital implementation of spiking neurons is more efficient than previous designs (supplementary section S3) and enables one-to-one correspondence between software and hardware (supplementary

¹IBM Research—Almaden, 650 Harry Road, San Jose, CA 95120, USA. ²IBM Research—Austin, 11501 Burnet Road, Austin, TX 78758, USA. ³Cornell University, 358 Upson Hall, Ithaca, NY 14853 USA. ⁴IBM Engineering and Technology Services, San Jose Design Center, 650 Harry Road, San Jose, CA 95120, USA. ⁵IBM Research—Tokyo, Nippon Building Fund Toyosu Canal Front Building, 5-6-52 Toyosu, Koto-ku Tokyo 135-8511, Japan. ⁶IBM T. J. Watson Research Center, 101 Kitchawan Road, Yorktown Heights, NY 10598, USA. ⁷Cornell Tech, 111 Eighth Avenue No. 302, New York, NY 10011, USA. *These authors contributed equally to this work. †Corresponding author. E-mail: dmodha@us.ibm.com

section S9). Mixed analog-digital as well as custom microprocessor-based neuromorphic approaches (13) have built event-driven communication frameworks (14) to emulate the interconnectivity of the brain by leveraging the speed of digital electronics. We have found that event-driven communication combined with colocated memory and computation mitigates the von Neumann bottleneck (15). Inspired by neuroscience (Fig. 2, A to C), our key architectural abstraction (Fig. 1C) is a network of neurosynaptic cores that can implement large-scale spiking neural networks that are efficient, scalable, and flexible within today's technology.

From a structural view, the basic building block is a core, a self-contained neural network with 256 input lines (axons) and 256 outputs (neurons) connected via 256-by-256 directed, programmable synaptic connections (Fig. 2D). Building on the local, clustered connectivity of a single neurosynaptic core, we constructed more complex networks by wiring multiple cores together using global, distributed on- and off-chip connectivity (Fig. 2, E and F). Each neuron on every core can target an axon on any other core. Therefore, axonal branching is implemented hierarchically in two stages: First, a single connection travels a long distance between cores (akin

to an axonal trunk) and second, upon reaching its target axon, fans out into multiple connections that travel a short distance within a core (akin to an axonal arbor). Neuron dynamics is discretized into 1-ms time steps set by a global 1-kHz clock. Other than this global synchronization signal, which ensures one-to-one equivalence between software and hardware, cores operate in a parallel and event-driven fashion (supplementary section S1). The fundamental currency that mediates fully asynchronous (16) intercore communication and event-driven intracore computation is all-or-nothing spike events that represent firing of individual neurons. The architecture is efficient because (i) neurons form clusters that draw their inputs from a similar pool of axons (17–19) (Fig. 2A) allowing for memory-computation colocalization (supplementary section S5); (ii) only spike events, which are sparse in time, are communicated between cores via the long-distance communication network; and (iii) active power is proportional to firing activity. The architecture is scalable because (i) cores on a chip, as well as chips themselves, can be tiled in two dimensions similar to the mammalian neocortex (Fig. 2, B and C); (ii) each spike event addresses a pool of neurons on a target

core, reducing the number of long-range spike events thus mitigating a critical bottleneck (supplementary section S4); and (iii) occasional defects at the core and chip level do not disrupt system usability. Last, the architecture is flexible because (i) each neuron is individually configurable, and the neuron model (20) supports a wide variety of computational functions and biologically relevant spiking behaviors; (ii) each synapse can be turned on or off individually, and postsynaptic efficacy can be assigned relative strengths; (iii) each neuron-axon connection is programmable along with its axonal delay; and (iv) the neurons and synapses can exhibit programmed stochastic behavior via a pseudo-random number generator (one per core). The architecture thus supports rich physiological dynamics and anatomical connectivity that includes feed-forward, recurrent, and lateral connections.

From a functional view, a core has individually addressable axons, a configurable synaptic crossbar array, and programmable neurons (Fig. 2G). Within a core, information flows from presynaptic axons (horizontal lines), through the active synapses in the crossbar (binary-connected cross-points), to drive inputs for all the connected postsynaptic neurons (vertical lines). Axons are

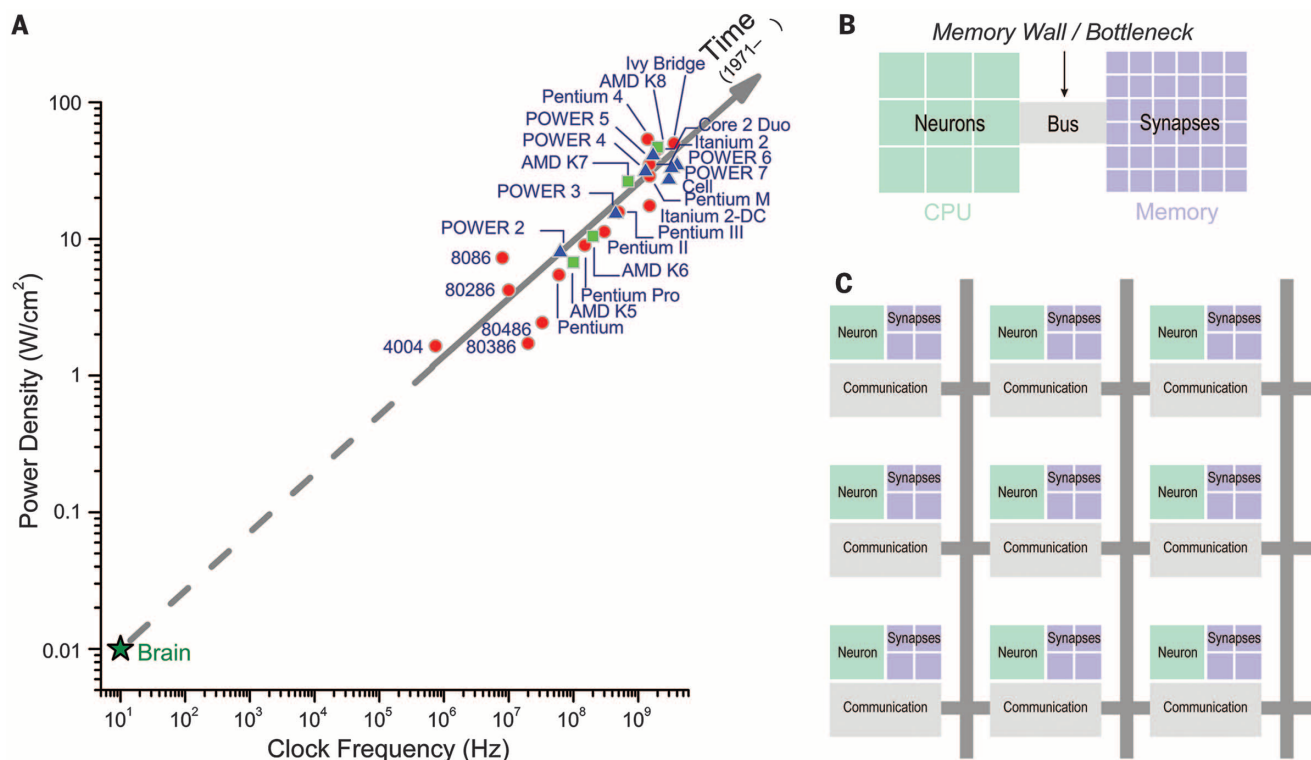


Fig. 1. Computation, communication, and memory. (A) The parallel, distributed architecture of the brain is different from the sequential, centralized von Neumann architecture of today's computers. The trend of increasing power densities and clock frequencies of processors (29) is headed away from the brain's operating point. Number and POWER processors are from IBM, Incorporated; AMD, Advanced Micro Devices, Incorporated; Pentium, Itanium, and Core 2 Duo, Intel, Incorporated. (B) In terms of computation, a single processor has to simulate both a large number of neurons as well as the inter-neuron communication infrastructure. In terms

of memory, the von Neumann bottleneck (15), which is caused by separation between the external memory and processor, leads to energy-hungry data movement when updating neuron states and when retrieving synapse states. In terms of communication, interprocessor messaging (25) explodes when simulating highly interconnected networks that do not fit on a single processor. (C) Conceptual blueprint of an architecture that, like the brain, tightly integrates memory, computation, and communication in distributed modules that operate in parallel and communicate via an event-driven network.

activated by input spike events, which are generated by neurons anywhere in the system and delivered after a desired axonal delay of between 1 and 15 time steps. Although the brain has a dedicated wire for each connection, in our architecture spike events are carried between cores by time-multiplexed wires (21) that interconnect a two-dimensional mesh network of routers, each with five ports (north, south, east, west, and local). The routers form the backbone of a two-dimensional mesh network interconnecting a 64-by-64 core array (Fig. 2H). When a neuron on a core spikes, it looks up in local memory an axonal delay (4 bits) and the destination address (8-bit absolute address for the target axon and two 9-bit relative addresses representing core hops in each dimension to the target core). This information is encoded into a packet that is in-

jected into the mesh, where it is handed from core to core—first in the x dimension then in the y dimension (deadlock-free dimension-order routing) until it arrives at its target core before fanning out via the crossbar (fig. S2). To implement feedback connections within a core, where a neuron connects to an axon on the same core, the packet is delivered by using the router's local channel, which is efficient because it never leaves the core. To scale the two-dimensional mesh across chip boundaries where the number of interchip connections is limited, we used a merge-split structure at the four edges of the mesh to serialize exiting spikes and deserialize entering spikes (Fig. 2I). Spikes leaving the mesh are tagged with their row (for spikes traveling east-west) or column (for spikes traveling north-south) before being merged onto a shared link

that exits the chip. Conversely, spikes entering the chip from a shared link are split to the appropriate row or column by using the tagged information.

From a physical view, to implement this functional blueprint, we built TrueNorth, a fully functional digital chip (supplementary section S6) with 1 million spiking neurons and 256 million synapses (nonplastic). With 5.4 billion transistors occupying 4.3-cm² area in Samsung's 28-nm process technology, TrueNorth has ~428 million bits of on-chip memory. Each core has 104,448 bits of local memory to store synapse states (65,536 bits), neuron states and parameters (31,232 bits), destination addresses (6656 bits), and axonal delays (1024 bits). In terms of efficiency, TrueNorth's power density is 20 mW per cm², whereas that of a typical central processing

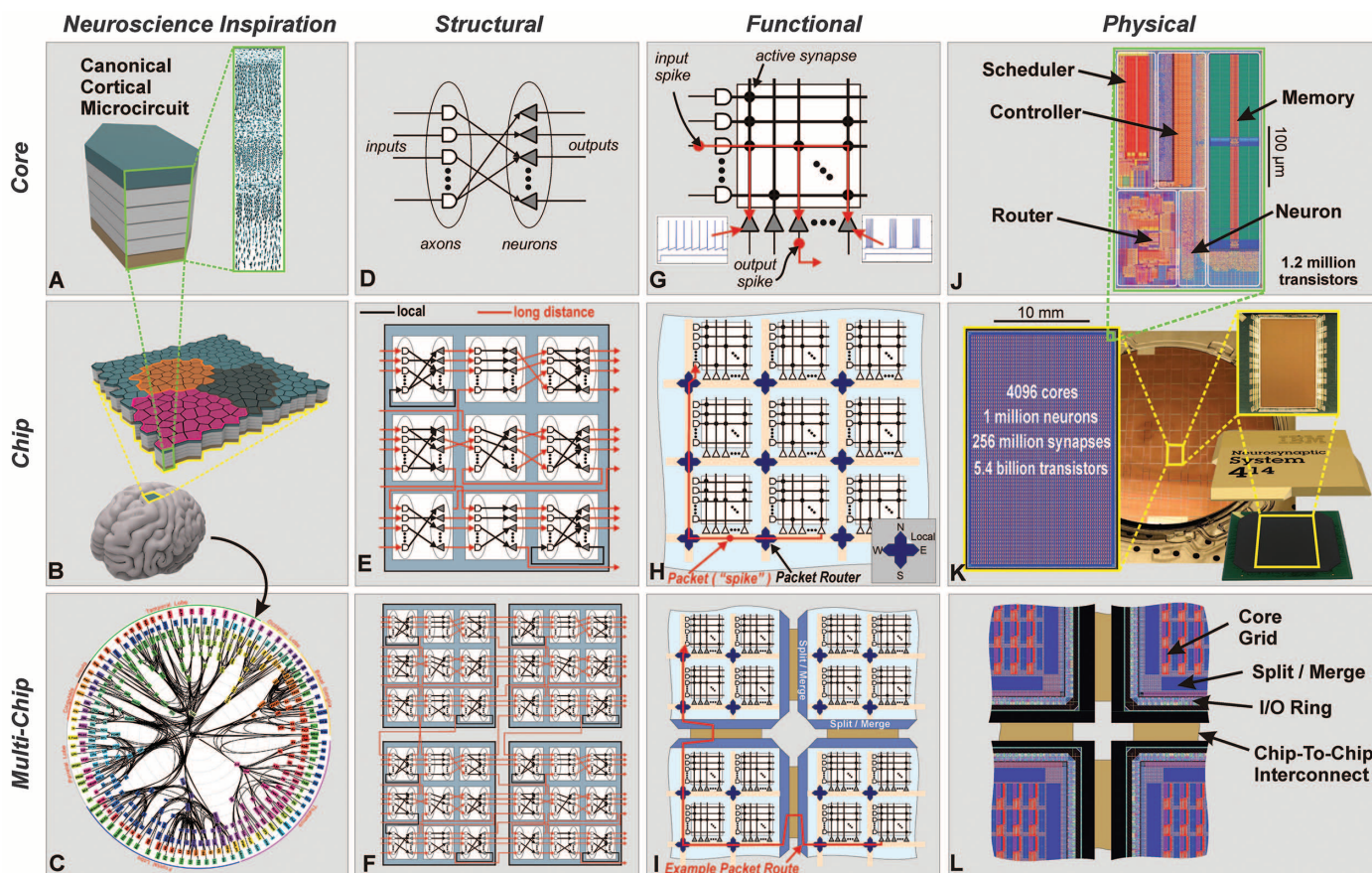


Fig. 2. TrueNorth architecture. Panels are organized into rows at three different scales (core, chip, and multichip) and into columns at four different views (neuroscience inspiration, structural, functional, and physical). (A) The neurosynaptic core is loosely inspired by the idea of a canonical cortical microcircuit. (B) A network of neurosynaptic cores is inspired by the cortex's two-dimensional sheet. (C) The multichip network is inspired by the long-range connections between cortical regions shown from the macaque brain (30). (D) Structure of a neurosynaptic core with axons as inputs, neurons as outputs, and synapses as directed connections from axons to neurons. Multicore networks at (E) chip scale and (F) multichip scale are both created by connecting a neuron on any core to an axon on any core with point-to-point connections. (G) Functional view of core as a crossbar where horizontal lines are axons, cross points are individually programmable synapses, vertical lines are neuron inputs, and triangles are neurons. Information flows from axons

via active synapses to neurons. Neuron behaviors are individually programmable, with two examples shown. (H) Functional chip architecture is a two-dimensional array of cores where long-range connections are implemented by sending spike events (packets) over a mesh routing network to activate a target axon. Axonal delay is implemented at the target. (I) Routing network extends across chip boundaries through peripheral merge and split blocks. (J) Physical layout of core in 28-nm CMOS fits in a 240- μ m-by-390- μ m footprint. A memory (static random-access memory) stores all the data for each neuron, a time-multiplexed neuron circuit updates neuron membrane potentials, a scheduler buffers incoming spike events to implement axonal delays, a router relays spike events, and an event-driven controller orchestrates the core's operation. (K) Chip layout of 64-by-64 core array, wafer, and chip package. (L) Chip periphery to support multichip networks. I/O, input/output.

unit (CPU) is 50 to 100 W per cm^2 (Fig. 1A). Active power density was low because of our architecture, and passive power density was low because of process technology choice with low-leakage transistors. This work advances a previous experimental prototype single neurosynaptic core (22)—scaling the number of cores by 4096 times and reducing core area by 15 times and power by 100 times. To enable an event-driven, hybrid asynchronous-synchronous approach, we were required to develop a custom tool flow, outside the scope of commercial software, for simulation and verification (supplementary section S2).

We used our software ecosystem (supplementary section S9) to map many well-known algorithms to the architecture (23) via offline learning, for example, convolutional networks, liquid state machines, restricted Boltzmann machines, hid-

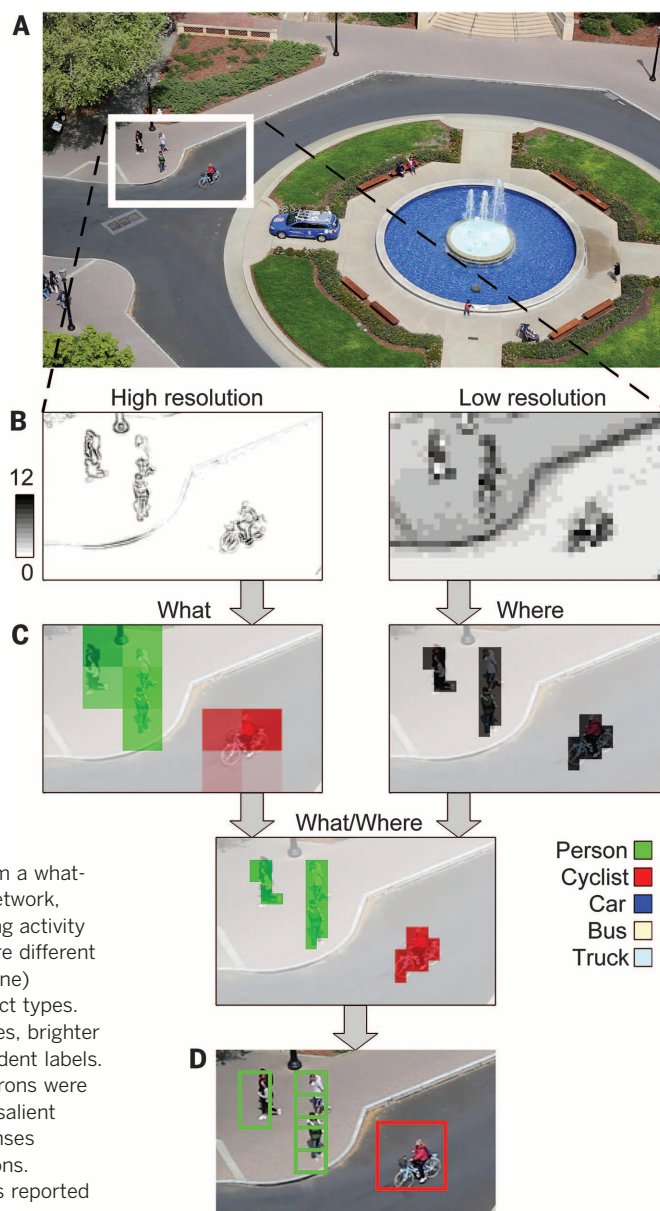
den Markov models, support vector machines, optical flow, and multimodal classification. These same algorithms now run without modification on TrueNorth. To test TrueNorth's applicability to real world problems, we developed an additional multiobject detection and classification application in a fixed-camera setting. The task had two challenges: (i) to detect people, bicyclists, cars, trucks, and buses that occur sparsely in images while minimizing false detection and (ii) to correctly identify the object. Operating on a 400-pixel-by-240-pixel aperture, the chip consumed 63 mW on a 30-frame-per-second three-color video (Fig. 3), which when scaled to a 1920-pixel-by-1080-pixel video achieved state-of-the-art performance (supplementary section S11). Because the video was prerecorded with a standard camera, we were required to convert the pixels into spike events to interface with TrueNorth. In

a live setting, we could use a spike-based retinal camera (12) similar to a previously demonstrated eye-detection application (23). We also implemented a visual map of orientation-selective filters, inspired by early processing in mammalian visual cortex (24) and commonly used in computer vision for feature extraction (supplementary section S10). All 1 million neurons received feed-forward inputs with an orientation bias from visual space as well as recurrent connections between nearby features to sharpen selectivity.

The standard benchmark of a computer architecture's efficiency is energy per operation. In the domain of configurable neural architectures, the fundamental operation is the synaptic event, which corresponds to a source neuron sending a spike event to a target neuron via a unique (nonzero) synapse. Synaptic events are the appropriate atomic units because the computation, memory, communication, power, area, and speed all scale with number of synapses. By using complex recurrently connected networks (Fig. 4A), we measured the total power of TrueNorth under a range of configurations (Fig. 4B) and computed the energy per synaptic event (Fig. 4C) (supplementary section S7). Power consumption in TrueNorth is a function of spike rate, the average distance traveled by spikes, and the average number of active synapses per neuron (synaptic density). At the operating point where neurons fire on average at 20 Hz and have 128 active synapses, the total measured power was 72 mW (at 0.775 V operating voltage), corresponding to 26 pJ per synaptic event (considering total energy). Compared with an optimized simulator (25) running the exact same network on a modern general-purpose microprocessor, TrueNorth consumes 176,000 times less energy per event (supplementary section S12). Compared with a state-of-the-art multiprocessor neuromorphic approach (13) (48 chips each with 18 microprocessors) running a similar network, TrueNorth consumes 769 times less energy per event (supplementary section S12). Direct comparison to these platforms is possible because, like TrueNorth, they support individually programmable neurons and connections, as required to run applications like our multiobject recognition example. Direct comparisons with other platforms is not possible because of different network constraints and system capabilities (supplementary section S13). Computation in TrueNorth is measured by using synaptic operations per second (SOPS), whereas in modern supercomputers it is floating-point operations per second (FLOPS). Although not a direct comparison, TrueNorth can deliver 46 billion SOPS per watt for a typical network and 400 billion SOPS per watt for networks with high spike rates and high number of active synapses (supplementary section S8), whereas today's most energy-efficient supercomputer achieves 4.5 billion FLOPS per watt.

We have begun building neurosynaptic supercomputers by tiling multiple TrueNorth chips, creating systems with hundreds of thousands of cores, hundreds of millions of neurons, and hundreds of billion of synapses. We envisage

Fig. 3. Real-time multi-object recognition on TrueNorth. (A) The Neovision2 Tower data set is a video from a fixed camera, where the objective is to identify the labels and locations of objects among five classes. We show an example frame along with the selected region that is input to the chip. (B) The region is transduced from pixels into spike events to create two parallel channels: a high-resolution channel (left) that represents the what pathway for labeling objects and a low-resolution channel (right) that represents the where pathway for locating salient objects. These pathways are inspired by dorsal and ventral streams in visual cortex (4). (C) What and where pathways are combined to form a what-where map. In the what network, colors represent the spiking activity for a grid of neurons, where different neurons were trained (offline) to recognize different object types. By overlaying the responses, brighter colors indicate more-confident labels. In the where network, neurons were trained (offline) to detect salient regions, and darker responses indicate more-salient regions. (D) Object bounding boxes reported by the chip.



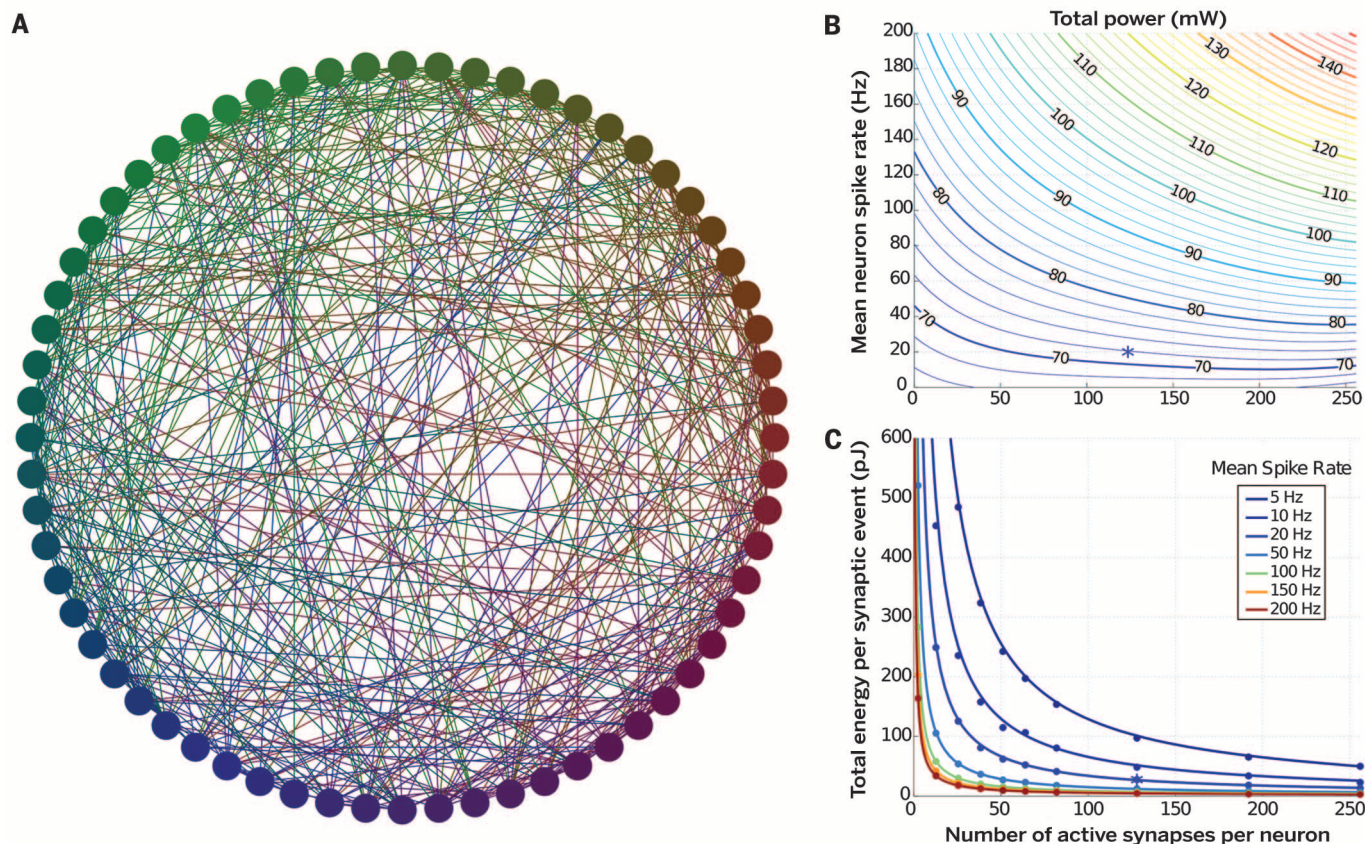


Fig. 4. Benchmarking power and energy. (A) Example network topology used for benchmarking power at real-time operation. Nodes represent cores, and edges represent neural connections; only 64 of 4096 cores are shown. (B) Although power remains low (<150 mW) for all benchmark networks, those with higher synaptic densities and higher spike rates consume more total power, which illustrates that power consumption scales

with neuron activity and number of active synapses. (C) The total energy (passive plus active) per synaptic event decreases with higher synaptic density because leakage power and baseline core power are amortized over additional synapses. For a typical network where neurons fire on average at 20 Hz and have 128 active synapses [marked as * in (B) and (C)], the total energy is 26 pJ per synaptic event.

hybrid computers that combine the von Neumann architecture with TrueNorth—both being Turing complete but efficient for complementary classes of problems. We may be able to map the existing body of neural networks algorithms to the architecture in an efficient fashion. In addition, many of the functional primitives of a recent large-scale complex behavioral model (3) map natively to our architecture, and we foresee developing a compiler to translate high-level functional tasks directly into TrueNorth networks. We envision augmenting our neurosynaptic cores with synaptic plasticity [see (26) for a prototype] to create a new generation of field-adaptable neurosynaptic computers capable of online learning. Although today TrueNorth is fabricated by using a modern complementary metal-oxide semiconductor (CMOS) process, the underlying architecture may exploit advances in future memory (27), logic (28), and sensor (12) technologies to deliver lower power, denser form factor, and faster speed.

REFERENCES AND NOTES

1. J. von Neumann, *The Computer and the Brain* (Yale Univ. Press, New Haven, CT, 1958).
2. C. Mead, *Analog VLSI and Neural Systems* (Addison-Wesley, Boston, MA, 1989).
3. C. Eliasmith et al., *Science* **338**, 1202–1205 (2012).
4. M. Mishkin, L. G. Ungerleider, K. A. Macko, *Trends Neurosci.* **6**, 414–417 (1983).
5. P. S. Churchland, T. J. Sejnowski, *The Computational Brain* (MIT Press, Cambridge, MA, 1992).
6. T. Yu, J. Park, S. Joshi, C. Maier, G. Cauwenberghs, in *Biomedical Circuits and Systems Conference (BioCAS)*, 2012 IEEE (IEEE, Los Alamitos, CA, 2012), pp. 21–24.
7. J. Schemmel et al., in *2012 IEEE International Symposium on Circuits and Systems (ISCAS)* (IEEE, Los Alamitos, CA, 2012), p. 702.
8. B. V. Benjamin et al., *Proc. IEEE* **102**, 699–716 (2014).
9. M. Mahowald, R. Douglas, *Nature* **354**, 515–518 (1991).
10. G. Indiveri et al., *Front. Neurosci.* **5** (2011).
11. R. H. Hahnloser, R. Sarpeshkar, M. A. Mahowald, R. J. Douglas, H. S. Seung, *Nature* **405**, 947–951 (2000).
12. S.-C. Liu, T. Delbruck, *Curr. Opin. Neurobiol.* **20**, 288–295 (2010).
13. E. Stamatias, F. Galluppi, C. Patterson, S. Furber, in *The International Joint Conference on Neural Networks (IJCNN)* (IEEE, Los Alamitos, CA, 2013), pp. 1–8.
14. M. Mahowald, *An Analog VLSI System for Stereoscopic Vision* (Kluwer Academic, Boston, 1994).
15. J. Backus, *Commun. ACM* **21**, 613–641 (1978).
16. J. Teifel, R. Manohar, in *Proceedings of 10th International Symposium on Asynchronous Circuits and Systems* (IEEE, Los Alamitos, CA, 2004), pp. 17–27.
17. R. J. Douglas, K. A. Martin, *Annu. Rev. Neurosci.* **27**, 419–451 (2004).
18. S. B. Laughlin, T. J. Sejnowski, *Science* **301**, 1870–1874 (2003).
19. V. B. Mountcastle, *J. Neurophysiol.* **20**, 408–434 (1957).
20. A. S. Cassidy et al., in *The International Joint Conference on Neural Networks (IJCNN)* (IEEE, Los Alamitos, CA, 2013), 10.1109/IJCNN.2013.6707077.
21. W. J. Dally, B. Towles, in *Design Automation Conference, 2001. Proceedings* (IEEE, Los Alamitos, CA, 2001), pp. 684–689.
22. P. Merolla et al., in *Custom Integrated Circuits Conference (CICC)*, 2011 IEEE (IEEE, Los Alamitos, CA, 2011), pp. 1–4.
23. S. K. Esser et al., in *The International Joint Conference on Neural Networks (IJCNN)* (IEEE, Los Alamitos, CA, 2013), 10.1109/IJCNN.2013.6706746.
24. D. H. Hubel, T. N. Wiesel, *J. Physiol.* **160**, 106–154 (1962).
25. R. Preissl et al., in *2012 International Conference for High Performance Computing, Networking, Storage and Analysis (SC)* (IEEE, Los Alamitos, CA, 2012), pp. 1–11.
26. J. Seo et al., in *Custom Integrated Circuits Conference (CICC)*, 2011 IEEE (IEEE, Los Alamitos, CA, 2011), pp. 1–4.
27. T. Ohno et al., *Nat. Mater.* **10**, 591–595 (2011).
28. M. M. Shulaker et al., *Nature* **501**, 526–530 (2013).
29. C. Isci, thesis, Princeton University, Princeton, NJ (2007).
30. D. S. Modha, R. Singh, *Proc. Natl. Acad. Sci. U.S.A.* **107**, 13485–13490 (2010).

ACKNOWLEDGMENTS

This research was sponsored by Defense Advanced Research Projects Agency (DARPA) under contract no. HRO011-09-C-0002. The views and conclusions contained herein are those of the authors and should not be interpreted as representing the official policies, either expressly or implied, of DARPA or the U.S. Government. U.S. patents 8473439 and 8515885 and U.S. patent applications 13/235,341 and 13/434,733 pertain to aspects of this work. We are grateful to many collaborators: A. Agrawal, A. Andreopoulos, S. Asaad, C. Baks, D. Barch, M. Beakes,

R. Bellofatto, D. Berg, J. Bong, T. Christensen, A. Cox, P. Datta, D. Friedman, S. Gilson, J. Guan, S. Hall, R. Haring, C. Haymes, J. Ho, S. Iyer, J. Krawiecki, J. Kusnitz, J. Liu, J. B. Kuang, E. McQuinn, R. Mousalli, B. Nathanson, T. Nayak, D. Nguyen, H. Nguyen, T. Nguyen, N. Pass, K. Prasad, M. Ohmacht, C. Ortega-Otero, Z. Saliba, D. L. Satterfield, J.-s. Seo, B. Shaw, K. Shimohashi, K. Shiraishi, A. Shokoubakhsh, R. Singh, T. Takken,

F. Tsai, J. Tierno, K. Wecker, S.-y. Wang, and T. Wong. We thank two anonymous reviewers for their thoughtful comments.

SUPPLEMENTARY MATERIALS

www.sciencemag.org/content/345/6197/668/suppl/DC1
Supplementary Text

Figs. S1 to S8
Tables S1 and S2
References (31–40)
Movie S1

10 April 2014; accepted 20 June 2014
10.1126/science.1254642

OIL BIODEGRADATION

Water droplets in oil are microhabitats for microbial life

Rainer U. Meckenstock,^{1,*†} Frederick von Netzer,¹ Christine Stumpp,¹ Tillmann Lueders,¹ Anne M. Himmelberg,¹ Norbert Hertkorn,² Philipp Schmitt-Kopplin,² Mourad Harir,² Riad Hosein,³ Shirin Haque,⁴ Dirk Schulze-Makuch^{5,6}

Anaerobic microbial degradation of hydrocarbons, typically occurring at the oil-water transition zone, influences the quality of oil reservoirs. In Pitch Lake, Trinidad and Tobago—the world's largest asphalt lake—we found that microorganisms are metabolically active in minuscule water droplets (1 to 3 microliters) entrapped in oil. Pyrotag sequencing of individual droplet microbiomes revealed complex methanogenic microbial communities actively degrading the oil into a diverse range of metabolites, as shown by nuclear magnetic resonance and Fourier transform ion cyclotron resonance mass spectrometry. High salinity and water-stable isotopes of the droplets indicate a deep subsurface origin. The 13.5% water content and the large surface area of the droplets represent an underestimated potential for biodegradation of oil away from the oil-water transition zone.

Petroleum hydrocarbons are excellent electron donors and carbon sources for microorganisms; therefore, they are readily degraded under oxic conditions. Albeit kinetically slower, anaerobic degradation of petroleum hydrocarbons also occurs with electron acceptors such as sulfate, nitrate, and ferric iron or under methanogenesis (1). Methanogenic degradation has been detected for oil reservoirs (2, 3), and although microorganisms are found throughout entire reservoirs (4), it is currently understood that the bulk of biodegradation processes are taking place at the oil-water transition zone (4, 5). Because oil wells usually produce pressurized water/oil suspensions containing disturbed microbial communities, such samples provide limited information on the habitat and processes in situ. We hypothesized that microbial life should be possible in the oil body itself, within water enclosures containing active microbial communities.

We collected undisturbed oil samples from Pitch Lake, the world's largest natural asphalt lake, in La Brea, Trinidad and Tobago (6) (fig. S1A). When oil samples were spread on aluminum foil, small bubbles were visible beneath the oil surface. Many bubbles contained gas and collapsed upon puncturing, whereas some contained entrapped water droplets of 1 to 3 μ l. Sampling and microscopic inspection of single water droplets showed that they indeed harbored microorganisms, some of which were actively motile under the microscope (fig. S1B). This observation substantiated that microbial life can exist in such microliter-scale water droplets entrained in oil, contrary to a previous hypothesis that the low water activity would impose water stress, making such environments too extreme for microbial life (7). However, the water activity in the droplets is much higher than in the surrounding oil. Furthermore, a dissolved ion analysis of bulk water showed that there were no obvious limitations for life caused by the lack of essential nutrients such as ammonia (95 mg/l) or phosphate (5 mg/l).

Bacterial communities of single water droplets and of bulk oil showed a diverse composition (Fig. 1). Pyrotags were dominated by members of the orders Burkholderiales and Enterobacteriales. Other prominent lineages present in the water droplets were the Bacteroidales, Rhodospirillales, Sphingomonadales, and to a lesser extent Thermotogales and Nitrosomonadales. The taxa identified in the water droplets were typical for oil samples (e.g., the Burkholderiales) and largely

consistent with an earlier characterization of solid samples from the Trinidad Pitch Lake (7) and also from a similar type of oil seep in California (8). A recent metagenomic investigation of samples from 10 oil reservoirs also identified similar taxa to be predominant (9). The repeated detection of 16S ribosomal RNA gene sequences of presumably aerobic, hydrocarbon-degrading populations such as the Burkholderiales in anoxic oil reservoirs might indicate heretofore unrecognized physiological features of these taxa. The sequences clustering within the Enterobacteriales in our study were of mostly unclassified affiliation.

Archaea were detectable in 7 of 12 analyzed droplets and consisted almost exclusively of known methanogens within the Methanosarcinales and Methanomicrobiales. These taxa indicate that acetotrophic and hydrogenotrophic methanogenesis play a role in the biodegradation of the pitch. In addition to these methanogenic archaea, halotolerant or halophilic Halobacteriales were also present in all archaea-positive water droplets, albeit at lower relative abundance. These organisms indicate a high salt origin of the water droplets, presumably from the formation water of the reservoir. The presence of methanogens suggests that methanogenesis was an important terminal electron-accepting process in the water droplets. The emitted gas on Pitch Lake, however, was dominated by thermogenic methane, with only a minor contribution of biogenic origin, as indicated by stable isotope ratios of carbon [-46.6 ± 0.2 per mil (‰)] and hydrogen (-169.4 ± 4.6 ‰) of methane extracted from the oil and respective reports in the literature (7, 10).

To determine the origin of the water droplets, we analyzed the dissolved ion composition as well as water-stable isotopes of bulk water samples from the oil. Both methods require water samples of >100 μ l and were therefore possible for water droplets extracted from the oil but not from single droplets. The water exhibited a near-neutral pH of 7.2 with salt concentrations similar to sea water (500 mM Na^+ , 536 mM Cl^-); these findings exclude rainfall or fresh surface water as a direct source of the droplets. Furthermore, surface water cannot disperse into the heavy oil phase without severe mechanical shearing. The elevated salt concentrations rather suggest a subsurface origin of the droplets with either seawater or brine influence, indicating that they must have been entrapped in the oil already in the reservoir or during the ascent.

A deep subsurface origin of the water droplets was also strongly supported by stable isotope analysis of the bulk water phases (Fig. 2). The $^{18}\text{O}/^{16}\text{O}$ and $^2\text{D}/^1\text{H}$ stable isotope ratios of the bulk water separated by gravitation and by

¹Institute of Groundwater Ecology, Helmholtz Zentrum München, 85764 Neuherberg, Germany. ²Research Unit Biogeochemistry, Helmholtz Zentrum München, 85764 Neuherberg, Germany. ³Department of Chemistry, Faculty of Science and Agriculture, University of the West Indies, St. Augustine Campus, Trinidad and Tobago. ⁴Department of Physics, Faculty of Science and Agriculture, University of the West Indies, St. Augustine Campus, Trinidad and Tobago. ⁵School of the Environment, Washington State University, Pullman, WA 99164, USA. ⁶Center for Astronomy and Astrophysics, Technical University Berlin, 10623 Berlin, Germany.
*Present address: Biofilm Center, University Duisburg-Essen, 45141 Essen, Germany. [†]Corresponding author. E-mail: rainer.meckenstock@uni-due.de